Numerical investigation on the flow around a square cylinder with an upstream splitter plate at low Reynolds numbers

Bo An · J. M. Bergadà · F. Mellibovsky · W. M. Sang · C. Xi

Abstract The present study focuses on the flow over a 2D square cylinder with a plate placed in front of it. An in-house code using the lattice Boltzmann method was employed for all the simulations presented. Few cases were simulated using the open source code *Nektar++*, the results obtained from both methodologies were compared. Regarding the plate, three related parameters, velocity ratio, distance between the plate and cylinder and the thickness of the plate, were studied in order to evaluate the impact of these parameters on the flow behavior. The interactions between these parameters were as well investigated. The effect of these parameters on flow transitional properties such as Hopf and Neimark–Sacker bifurcations were discussed. Whenever the velocity ratio exceeds a certain value, Kelvin–Helmholtz instabilities dominate the vortex shedding. As velocity ratio increases, drag coefficient and vortex shedding frequency increase. The POD method was employed to predict the flow behavior based on the existing information. It turned out the POD method is a trustable methodology to mathematically pre-investigate the flow field, therefore it is capable of saving large computational resources.

List of symbols

$\vec{a}$	Acceleration of molecules
A_{ii}	Correlated matrix
c_s	Sound speed
c	Lattice velocity
$Cd - mean$	Mean value of drag coefficient
$Cd - A$	Amplitude of drag coefficient
D	Space dimension
D^*	Distance between the cylinder and plate
d_D	Particle diameter
$\vec{e}_\alpha$	Unit velocities vector along discrete directions
$\vec{g}$	The vertical component of velocity vector difference
$f(\vec{r}, \vec{\xi}, t)$	Distribution function

B. An (✉) · J. M. Bergadà
Department of Fluid Mechanics, Universitat Politécnica de Catalunya, 08034 Barcelona, Spain
e-mail: bo_alan_an@163.com

F. Mellibovsky
Department of Physics, Aerospace Engineering Division, Universitat Politécnica de Catalunya, 08034 Barcelona, Spain

W. M. Sang
School of Aeronautics, Northwestern Polytechnical University, Xi'an, China

C. Xi
Chinese Flight Test Establishment, Xi'an, China

$f^{eq}(\vec{r}, \vec{\xi})$	Equilibrium distribution function
F_1, F_2	Post-collision distribution function of two fluid particles
f_1, f_2	Pre-collision distribution function of two fluid particles
f_α	Discrete distribution functions on α directions
F_α	Discrete distribution functions on α directions after collision
$f_\alpha(\vec{r} + \vec{e}_\alpha \Delta t, t + \Delta t)$	Discrete—post collision distribution functions vector
$f_\alpha(\vec{r}, t)$	Discrete—pre collision distribution functions vector
$\vec{f}_\alpha^{eq}$	Nine-ordered vector of discrete equilibrium distribution functions
f_α^{neq}	The non-equilibrium state of distribution functions
L	Characteristic length (edge)
L_v	Vortex length for steady flow
M	The number of data blocks
m_i	Combinations of parameters (blocks of data)
N	The number of snapshots
Re	Reynolds number
r^*	Velocity ratio
$\vec{r}$	Spatial position vector
t	Time
Tk^*	Thickness of the plate
$\vec{u}$	Macroscopic quantity, velocity
U	Initial velocity component in horizontal direction
u	Velocity component in horizontal direction
v	Velocity component in vertical direction
$\vec{v}_j$	Eigenvector obtained from correlated matrix
$y(x_j, m_i)$	A physical field
y^+	Non-dimensional wall distance
Δx	Grid spacing
Δt	Time step
ε	Average thickness of the flapping layer on the upper cylinder surface
$\left[\delta_i(m_j)\right]_{M \times M}$	Empirical coefficient matrix
$\phi^i(x_j)$	Base vectors
λ	Eigenvalue
ρ	Macroscopic quantity, density
τ	Single relaxation time term
Ω_f	Collision operator
Ω_f^α	Discrete collision operator on α directions
$d\Theta$	Integral infinitesimal of angle
ω_α	Weight Coefficients
$\vec{\xi}$	Velocity vector of molecules

1 Introduction

1.1 Passive flow control of the flow over a square cylinder

During the past few decades, investigations about flow around bluff bodies have always been a hot topic in computational fluid dynamics, not just in theoretical studies but also in practical applications. Specifically, the circular and square cylinders under laminar flow conditions, see references [1–3] and [4–11] respectively, were well studied for more than a half century using both experimental and computational means. Tritton [1] launched some experiments on the flow around a circular cylinder at Reynolds numbers ranging from 0.5 to 100, body forces were measured and the vortex shedding process was also captured. Braza et al. [2] numerically studied the pressure and velocity fields of the unsteady incompressible laminar wake behind a circular cylinder by using the second order accuracy finite volume method, body forces were calculated at Reynolds numbers 100, 200 and 1000. Allicvi and Bermejo [3] performed a numerical study on the flow past a cylinder via using the finite element modified method, lift and drag coefficients at Reynolds number 100 were presented. Regarding the square cylinder, Okajima [4] performed a series of experiments finding out the Strouhal number associated to each Reynolds number and as a function of width-to-height ratio of the rectangular cylinders. The Reynolds number was varied from 70 to 2×10^4, width-to-height ratio varied from 1 to 4. The experimental results were confirmed by numerical calculations. Kelkar and Patankar [5] investigated the 2D flow around a square cylinder at different Reynolds numbers via using linear stability analysis. The onset of

unsteadiness was studied and analyzed through various time-stepping techniques, the main purpose was to determine the most appropriate technique for studying the perturbations growth. A simulation at Reynolds number beyond the critical value was also performed to find out the periodic characteristics of the flow. They found the critical Reynolds number between steady and unsteady flow was 53. In 1995, Sohankar et al. [6] investigated the laminar flow around a square cylinder at Reynolds numbers ranging from 45 to 250. For each Reynolds number tested, they predicted the lift, drag, pressure coefficient and Strouhal number. It turned out that at Reynolds number 55, the flow exhibited a well-defined vortex shedding frequency but at Reynolds number 50 the flow was still steady. Four years later, Sohankar et al. [7] undertook another study on flow around a 3D square cylinder at moderate Reynolds numbers, where based on their experiments [8] they reported that the steady/unsteady Reynolds critical value was 47 ± 2, from the simulations performed, they observed the Reynolds number at which the flow became 3D was between 150 and 200. Luo et al. [9] investigated experimentally the flow transition in the wake of a square cylinder. In their study they determined two different unstable modes, modes A and B, their respective Reynolds numbers associated were 188–190 and 230–260. They concluded that the vortex formation mechanism in circular and square cylinders was the same, due to the similar vortical structures they observed between corresponding modes for these two bluff bodies. In 2009, Ul-Islam and Zhou [10] investigated the flow around a square cylinder at Reynolds number 100 via using the lattice Boltzmann method, the aim was to determine the influence of the different boundary conditions on the downstream flow characteristics. In the same year, Ali et al. [11] conducted a grid convergence study for 2D flow around a square cylinder at Reynolds number 150. They noticed that the grid independency was achieved when the first cell was placed at a non-dimensional distance of 0.005 from the solid surface.

Recently, the flow control technology has been applied to the flow over bluff bodies, most of the work refers to the passive flow control [12–18], where the flow is being modified via using static devices, being this the kernel idea of passive flow control. In 1998, Sohankar et al. [12] conducted several simulations on the flow around a square cylinder by introducing an adjustable parameter, angle of attack (*AOA*), ranging from 0 to 45. They observed when using a null value of *AOA*, that the critical Reynolds number was found to be 51.2 ± 1.0. For the full range of the *AOA* studied angles, $[0, 45]$, the onset of unsteadiness occurred within the Reynolds number interval $(40, 55)$. Zhou et al. [13] researched the flow around a square cylinder with a control plate upstream. They placed a vertical plate in front of the square cylinder and introduced the height of the plate as a changeable parameter, they investigated its influence on the downstream vortex shedding wake. Cheng et al. [14] performed a series of calculations via using the lattice Boltzmann method, to study the flow characteristics of a linear shear flow past a square cylinder at Reynolds numbers from 50 to 200. The authors presented a controllable parameter known as shear rate, via modifying such parameter, at $Re = 50$ they noticed the steady flow could be disturbed and turned into unsteady. Doolan [15] investigated the interaction between a square cylinder and a horizontal downstream detached plate at $Re = 150$. In his study, the 2D N-S equations were solved using the finite volume methodology implemented in OpenFOAM. He reported the perturbation caused by the plate could bring a non-negligible influence on the Strouhal number and force coefficients. In Ali et al. [16], they investigated a square cylinder with a splitter plate attached to the rear, they introduced the plate length as a modifiable parameter. Numerically, they discovered that the splitter plate can fundamentally change the flow structure of the wake. Ul-Islam et al. [17] performed a similar study but with a thick detached splitter plate. In their study, they took the distance between the square cylinder and the plate as a modifiable parameter. In 2016, Wang et al. [18] presented a study on the flow around a square cylinder, with a porous vertical plate near the wake. They concluded that the drag coefficient decreased to some extent compared with the one associated to the cylinder without a plate. The Strouhal number was also reduced and under some conditions the vortex shedding could even be suppressed.

In the present study, a horizontal splitter plate was placed upstream of a square cylinder. Four parameters, velocity ratio r^*, distance between cylinder and plate D^*, thickness of the plate Tk^* and Reynolds number Re, were evaluated. The maximum value of Reynolds number below the splitter plate is 56, being this maximum value of the Reynolds number based on the

velocity above the plate 224. As it will be explained in the results section, these four parameters have a deep impact on the flow topology, vortex shedding frequency, amplitude and drag forces acting on the cylinder. The critical Reynolds numbers at which Hopf and Neimark–Sacker bifurcations appear are affected by these four parameters. Having four adjustable parameters under consideration, and in order to properly study the impact of each parameter, a large amount of simulations need to be performed, being very expensive computationally, especially when considering the large mesh (19,800,000 cells) used in present study. Therefore, in the present paper, it was employed a mathematical algorithm known as the proper orthogonal decomposition (POD) to predict with a tolerant error, the flow field characteristics under any combination of the controllable parameters. It is important to notice that the square cylinder with a splitter plate located upstream was just investigated in Ref. [26], where just some velocity ratios were numerically studied in 2D, although at some of the Reynolds numbers studied the flow should have been considered as 3D. In the present paper, for all Reynolds number studied the flow is two dimensional, this is why all simulations were performed in 2D. The entire information presented in this paper is novel and can not be found elsewhere.

The paper is structured as follows, Sects. 2, 3 and 4 are respectively focusing on the mathematical background for LBM and POD, mesh and boundary conditions for the LBM simulations, and LBM code validation. Section 5 is devoted to the results, in Sects. 5.1 to 5.3, LBM is employed to investigate the influence of four parameters on the flow physics. In Sect. 5.4, initially further LBM simulations were done to be able to generate the different sample matrixes to predict the new results by using the POD method. For each predicted result using POD, a new LBM simulation was done to compare the results with the predicted ones. The final part of the paper summarizes the main conclusions obtained.

2 Mathematical background

2.1 Lattice Boltzmann method (LBM)

In what follows, a brief description of the original LBM is presented. The continuous Boltzmann

equation is given by Eq. (1), notice that all parameters presented in this equation, as well as the ones introduced in all equations presented in this paper are non-dimensional.

$$\frac{\partial f(\vec{r}, \vec{\xi}, t)}{\partial t} + \vec{\xi} \cdot \frac{\partial f(\vec{r}, \vec{\xi}, t)}{\partial \vec{r}} + \vec{a} \cdot \frac{\partial f(\vec{r}, \vec{\xi}, t)}{\partial \vec{\xi}}$$
$$= \iint (F_1 F_2 - f_1 f_2) d_D^2 |\vec{g}| \cos\theta d\Theta d\vec{\xi}_1 \qquad (1)$$

The left hand side of Eq. (1) represents the streaming term, the right hand side represents an integral–differential term, which is called the collision term. Simplified by Bhatnagar–Gross–Krook (BGK) operator, Eq. (1) reads as

$$\frac{\partial f(\vec{r}, \vec{\xi}, t)}{\partial t} + \vec{\xi} \cdot \frac{\partial f(\vec{r}, \vec{\xi}, t)}{\partial \vec{r}} + \vec{a} \cdot \frac{\partial f(\vec{r}, \vec{\xi}, t)}{\partial \vec{\xi}} = \Omega_f$$
$$= \frac{1}{\tau} [f^{eq}(\vec{r}, \vec{\xi}) - f(\vec{r}, \vec{\xi}, t)] \qquad (2)$$

where τ is the singular relaxation time term and $f^{eq}(\vec{r}, \vec{\xi})$ is the equilibrium distribution function.

Discretizing Eq. (2) both on space and time, the lattice Boltzmann equation is obtained and given by Eq. (3)

$$f_\alpha(\vec{r} + \vec{e}_\alpha \Delta t, t + \Delta t) - f_\alpha(\vec{r}, t) = \Omega_f^\alpha$$
$$= \frac{1}{\tau} [f_\alpha^{eq}(\vec{r}, \vec{\xi}) - f_\alpha(\vec{r}, \vec{\xi}, t)] \qquad (3)$$

where α represents the direction of discrete velocities, $f_\alpha(\vec{r} + \vec{e}_\alpha \Delta t, t + \Delta t)$ and $f_\alpha(\vec{r}, t)$ are the discrete -post and -pre collision distribution functions vector and Ω_f^α is the discrete collision operator on α directions. The relation between the molecular movements and flow filed, in the present study, is introduced in Eq. (4)

$$\begin{cases} \rho = \sum_\alpha f_\alpha \\ \rho \vec{u} = \sum_\alpha \vec{e}_\alpha f_\alpha \end{cases} \qquad (4)$$

where ρ is the fluid density and $\vec{u}$ represents velocity field.

According to the LBGK model [19], the equilibrium distribution functions, for the 9 discrete velocities (9-bit model), are determined by

$$f_\alpha^{eq} = \omega_\alpha \rho [1 + \frac{\vec{e}_\alpha \cdot \vec{u}}{c_s^2} + \frac{(\vec{e}_\alpha \cdot \vec{u})^2}{2c_s^4} - \frac{u^2}{2c_s^2}]$$
$$\alpha = 0, 1, \ldots, 8 \qquad (5)$$

where ω_α are the weight coefficients, and c_s is the non-

dimensional sound speed. The discrete velocities of LBGK two dimensional 9-bit model *D2Q9* are given by

$$\vec{e} = c \begin{bmatrix} 0 & 1 & 0 & -1 & 0 & 1 & -1 & -1 & 1 \\ 0 & 0 & 1 & 0 & -1 & 1 & 1 & -1 & -1 \end{bmatrix}$$

$$c_s = \frac{c}{\sqrt{3}} \ \omega_\alpha = \begin{cases} 4/9 \ \vec{e}_\alpha^2 = 0 \\ 1/9 \ \vec{e}_\alpha^2 = c^2 \\ 1/36 \ \vec{e}_\alpha^2 = 2c^2 \end{cases}$$

$$(6)$$

where $c = \Delta x / \Delta t = 1$ is the non-dimensional lattice velocity, Δx and Δt are the lattice grid non-dimensional spacing and the non-dimensional time step respectively.

Figure 1 shows the discrete velocities of the LBGK *D2Q9* model employed in all simulations presented in this paper.

2.2 Proper orthogonal decomposition (POD)

The proper orthogonal decomposition (POD), as a post-processing algorithm, was introduced in physical applications four decades ago, the original and elementary investigation was performed by Lumley [20] and Sirovich [21]. According to Lumley, POD is a very efficient tool to predict the dominant representation of a physical field with a finite number of data blocks. The basic idea of POD is obtaining the best orthogonal basis from the existing data via performing an orthogonal transformation of the sample covariance matrix, then with the best orthogonal basis, the physical domain will be reconstructed with a tolerant residual. The snapshots method introduced in Sirovich's work [21] is also used in the present study, due to its efficiency and convenience. In Ref. [22], Liang

Fig. 1 Discrete velocities of lattice Boltzmann *D2Q9* model

et al. presented a study about the introduction of some of the different kinds of POD, Karhunen–Loeve decomposition (KLD), principal component analysis (PCA), and singular value decomposition (SVD), as well as their applications. In 1996, Holmes et al. [23] introduced the POD in turbulence studies of computational fluid dynamics (CFD) applications. In the present study, the snapshots POD approach, first introduced by Sirovich [21], is coupled with a cubic spline interpolation procedure to develop reliable, fast, low-order models for accurately predicting flow fields for the different parameters involved in this study. In what follow, a brief introduction of the snapshots POD method employed in the present paper will be presented.

Theoretically, any kind of physical field can be represented in the form of a finite series, as shown in Eq. (7).

$$\begin{aligned} y(x_j, m_i) &= \sum_{i=1}^M \delta_i(m_i)\phi^i(x_j), \ i = 1, \ldots, M, \ j \\ &= 1, \ldots, N \end{aligned} \tag{7}$$

where, $y(x_j, m_i)$ represents a physical field for a given domain under a given status (a data block), x_j represent any physical quantity, like velocity, pressure or temperature, m_i describes different combinations of parameters (blocks of data) characterizing the physical field. In the present paper, the parameters include Reynolds numbers, plate thickness, velocity ratio and plate position, M is the number of the data blocks, $\delta_i(m_i)$ are the empirical coefficients and $\phi^i(x_j)$ refers to the base vectors. For each block, the physical field forms a column vector $\vec{y}_i = [y(x_1, m_i), y(x_2, m_i), \ldots, y(x_N, m_i)]^T$ with N elements, where N is the length of each block, also known as the number of snapshots. With all the data blocks together, a $N \times M$ matrix $[y(x_j, m_i)]_{N \times M}$ is obtained, which is also known as the sample matrix. To predict a new physical quantity, the POD method requires to start with a sample matrix, the data of this matrix is obtained based on previous information, which are the physical quantities obtained through simulation or experimentation.

According to the POD theory, the empirical coefficients $\delta_i(m_i)$ and the base vectors $\phi^i(x_j)$ extracted from the sample matrix, must satisfy Eq. (8), which finally leads to an eigenvalue problem [24] shown in Eq. (9).
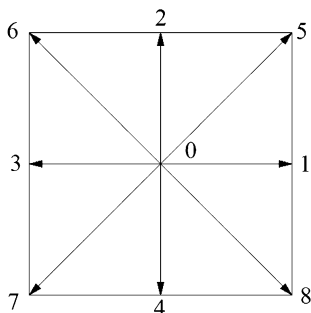
$$Maximize \left\{ \lambda = \frac{\left\langle (\phi(x_j), y(x_j, m_i))^2 \right\rangle}{(\phi(x_j), \phi(x_j))} \right\} \quad (8)$$

where, $\langle , \rangle$ denotes the averaging operation, $(,)$ refers to the Euclidean inner product and λ is the eigenvalue.

$$\int_\Omega \left\langle y(x_j, m_i), y(x_j', m_i) \right\rangle \phi(x_j') dx_j' = \lambda \phi(x_j') \quad (9)$$

where, $\left\langle y(x_j, m_i), y^*(x_j', m_i) \right\rangle = \frac{1}{M} \sum\limits^{M} y(x_j, m_i) y^* (x_j', m_i)$ is the averaged auto-correlation function, $y^*(x_j', m_i)$ denotes the Hermitian matrix of $y(x_j, m_i)$.

The snapshots POD method, makes easier to solve the eigenvalue problem addressed in Eq. (9), by introducing the idea that base vectors are actually a linear combination of snapshots. Therefore, the eigenvalue problem has been reduced and simplified to solve the eigenvalues of a correlated matrix A_{ii}, where

$$A_{ii} = (y(x_j, m_i))^{\mathrm{T}} \times (y(x_j, m_i)) \quad i = 1, 2, \ldots, M$$
$$j = 1, 2, \ldots, N \quad (10)$$

Notice that the correlated matrix A_{ii} is obtained when multiplying the transpose sample matrix by the sample matrix. From the correlated matrix A_{ii} the eigenvalues and eigenvectors are obtained. To determine the base vectors, Eq. (11) is employed, this equation clarifies that the base vectors are obtained when multiplying the sample matrix $y(x_j, m_i)$ by the column eigenvectors $\vec{v}_j$.

$$\phi^i(x_j) = \left(y(x_j, m_i), \vec{v}_j \right) \quad (11)$$

To obtain the empirical coefficients based on the sample matrix, it is required to multiply the transpose sample matrix by the base vectors as defined in Eq. (12)

$$\left[\delta_i(m_j) \right]_{M \times M} = \left(y(x_j, m_i)^{\mathrm{T}}, \phi^i(x_j) \right) \quad (12)$$

At this point, the empirical coefficient matrix $\left[\delta_i(m_j) \right]_{M \times M}$, $i = 1, \ldots, M$, $j = 1, \ldots, M$, and the base vectors have been obtained. The left and right hand side of Eq. (7) are known. In order to build the aiming block (block No. $M + 1$), it is required to interpolate the empirical coefficients of the block $M + 1, \delta_i (m_{M+1})$, in each coefficient column, afterwards the physical field of this new block (block No. $M + 1$)

will be obtained by using Eq. (13). Notice that the base vectors were obtained using Eq. (11).

$$y(x_j, m_{M+1}) = \sum\nolimits_{i=1}^{M} \delta_i(m_{M+1}) \phi^i(x_j),$$
$$i = 1, \ldots, M, \; j = 1, \ldots, N \quad (13)$$

3 Mesh and boundary conditions

Figure 2 states the physical problem and boundary conditions employed in the present geometry. The domain considered in the present application consists of a square cylinder located downstream of a detached splitter plate. At the inlet, the velocity fields below and above the plate are related by a given velocity ratio, r^*. Providing the square cylinder characteristic length is L, the distance between the plate and the cylinder is initially $3.0L$, being the splitter plate length also $3.0L$. The outlet is located at a distance of $24.0L$ downstream of the square cylinder, the upper and lower boundaries are located at a distance $8.0L$ from the cylinder centre line. For further information of why such distances were chosen it is recommended to see Sohankar et al. [12], where they clarified that under laminar conditions such distances are required to make sure that boundaries do not affect the internal flow. A set of different cases involving several Reynolds numbers, splitter-plate square cylinder distances, different velocity ratios and different splitter plate thicknesses were evaluated, over 150 cases were simulated. Boundary conditions are a key point in CFD, having a crucial influence on the computational results. As can be seen in Fig. 2, for the up and down far-field boundaries as well as for the outlet, Neumann
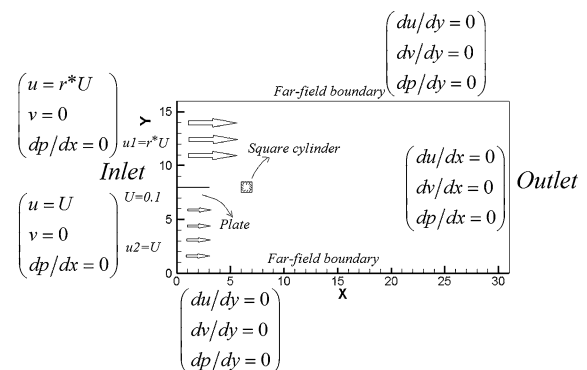
Fig. 2 Physical domain and boundary conditions

boundary conditions were employed for all flow quantities. At the inlet, Dirichlet boundary conditions for velocities u and v were employed, Neumann boundary conditions for pressure were used. Notice that the component of the velocity towards the x direction above the splitter plate is defined as r^* times the same component of the velocity below the splitter plate. In all solid boundaries, non-slip boundary conditions for velocities u and v were employed, Neumann boundary conditions for pressure were used. It is interesting to realize that the boundary conditions for pressure, are in reality given as boundary conditions for density, in LBM and for incompressible flow, the relation between pressure and density is given as $p = \rho/3$.

The application of standard Cartesian grid is very common in LBM, because of its particular structural advantages that fit the streaming-collision theory of LBM. Figure 3 shows the standard Cartesian mesh employed for the present application. On the left hand side, the full domain is presented, the total number of cells was 19,800,000 and the grid spacing was 0.005, the right hand side of Fig. 3 presents a zoomed view of the mesh. Regarding the *Nektar++*, a non-uniform structured grid having 121,198 cells was employed.

In the current numerical cases, the non-equilibrium extrapolation scheme [25] is employed to define the inlet, outlet, solid and far-field boundary conditions. The basic idea behind this scheme is that the distribution function of each direction can be classified into two parts, known as the non-equilibrium term and the equilibrium term.

As shown in Fig. 4, the grid nodes A, B and C are flow points, the grid nodes D, E and F are boundary points (inlet, outlet, solid and far-field). For points
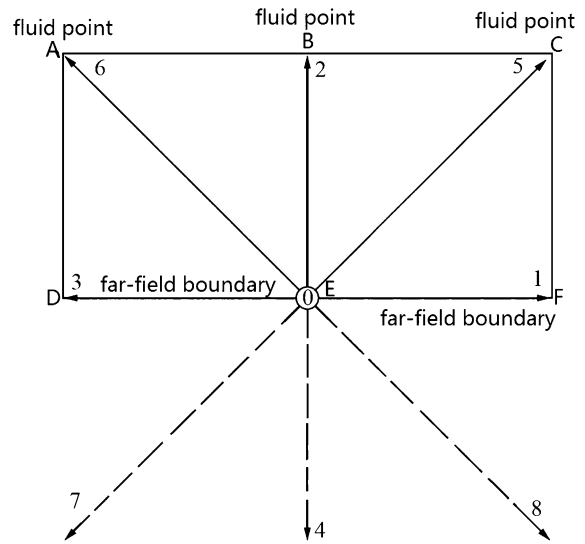

Fig. 4 Spatial discretization to be used in the inlet, outlet, solid and far-field boundaries

E and B, the distribution function of each direction is written as

$$f_\alpha(E,t) = f_\alpha^{eq}(E,t) + f_\alpha^{neq}(E,t) \tag{14}$$

$$f_\alpha(B,t) = f_\alpha^{eq}(B,t) + f_\alpha^{neq}(B,t) \tag{15}$$

The equilibrium part $f_\alpha^{eq}(E,t)$ is obtained from the macroscopic quantities of point E. While, the non-equilibrium distribution functions of point E can be replaced by the homologous of point B.

$$f_\alpha^{neq}(E,t) \approx f_\alpha^{neq}(B,t) \tag{16}$$

Hence, the distribution functions of point E become

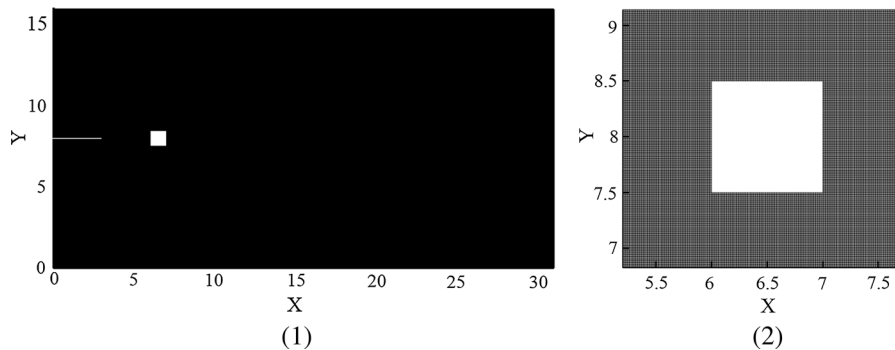$$f_\alpha(E,t) = f_\alpha^{eq}(E,t) + f_\alpha(B,t) - f_\alpha^{eq}(B,t) \tag{17}$$

Fig. 3 Uniform Cartesian mesh used to evaluate the flow around a square cylinder

4 Code validation

In this section, the present code was validated at three different Reynolds numbers, 50, 52 and 150, the splitter plate was not considered in these validation cases. Tables 1 and 2 compare some of the results obtained using the present code with the ones obtained from previous investigations. Table 1 compares the downstream bubble lengh at two different Reynolds numbers, 50 and 52, gathered from the present simulation and from references [6, 26], notice that under these conditions there is no vortex shedding. Table 2 compares the average drag coefficient and the Strouhal number at Reynolds 150 obtained from the present simulations, using LBM and *Nektar++*, with the references [7, 11, 15]. Based on the results presented in these two tables it can be concluded that, within the Reynolds numbers studied, the in-house code generated has a very good degree of accuracy. Notice that the same boundary conditions and the minimum value of grid spacing were used for both simulations, LBM and *Nektar++*. The maximum value of y^+ at Reynolds number 150 was found to be 0.544.

From these initial simulations it was stated that at $Re = 150$, the flow is unsteady with periodic vortex shedding. Notice that in Ref. [11, 18], the smallest grid spacing was respectively of 0.0667 and 0.01, clearly the grid spacing used in the present LBM simulations, which is of 0.005, allows to obtain a higher degree of precision. Figure 5 presents a full period of the vortex shedding process. It is interesting to observe that the vortices grow alternatively from the downstream upper and lower corners, and are being shed downstream in a typical Von Karman vortex street.

5 New results and analysis

The results about to be presented are divided in four main subsections, initially all cases will be analyzed via directly modelling the flow using LBM. On a second step and based on the results obtained from the initial modelling, the POD method will be used to extrapolate results for other cases not considered in the first section. As a final section, some of the cases extrapolated via POD will be fully simulated using LBM and the comparison of the results obtained when employing both methodologies will be undertaken.

5.1 Evaluation of the splitter plate-square cylinder distance effect on the flow field

In the present section, LBM simulations were performed to find out the critical Reynolds numbers characterizing the Hopf bifurcation for three different splitter-plate-square-cylinder distances, CFD simulations using the open source, *Nektar++* package were as well performed to compare with LBM results. The parameters remaining constant were, the splitter plate thickness $Tk^* = 0.0L$ and the velocity ratio $r^* = 1.0$. It is expected that, as the Reynolds number increases, the flow field changes from laminar steady to laminar unsteady periodic, followed by unsteady quasi-periodical and finally goes to chaotic. According to the investigation performed by Sohankar et al. [7], the flow around a square cylinder is starting to show 3D characteristics at Reynolds numbers between 150 and 200, indicating that the present study based on a 2D model is appropriate. In fact, studies undertaken by the present researchers indicate that for a square cylinder without a plate and affected by a constant velocity upstream, at Reynolds number 163 three dimensional structures start appearing. In references [6, 12], Sohankar et al. observed that the first critical Reynolds number, characterizing the boundary between steady and unsteady periodic flow, for a square cylinder without the splitter plate, was respectively 52 and 51.2 ± 1.0. In the present study, it was found that the critical Reynolds number between steady and unsteady periodic, for square cylinder was 53, when using a convergence criterion of 10^{-6}. When studying

Table 1 The comparison of the flow parameters at Reynolds 50 and 52

	Data source	This paper LBM	Ref [6].	Ref [26].
Re = 50	L_v/L	3.726	3.55	3.68
Re = 52	L_v/L	4.089	–	4.1

Table 2 The comparison of the flow parameters at Reynolds 150

Data source	This paper LBM	This paper $Nektar++$	Ref [7].	Ref [15].	Ref [18].	Ref [11].
$Cd - mean$	1.5411	1.54	1.44	1.44	1.4737	1.47
St	0.16102	0.162	0.165	0.156	0.160	0.160

(1) t0=13.0217s   *(2) t1=13.0397s*   *(3) t2=13.0576s*

(4) t3=13.0756s   *(5) t4=13.0936s*   *(6) t5=13.11148s*
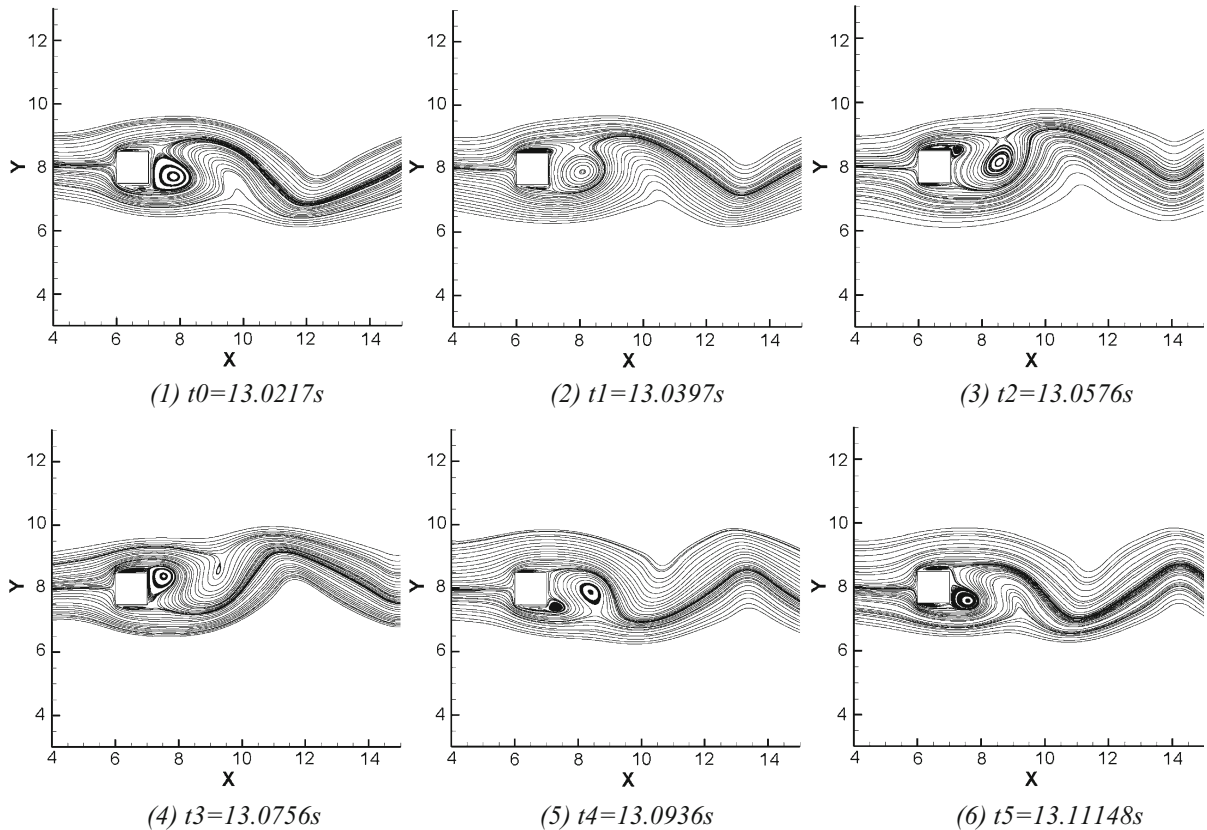
Fig. 5 Streamlines of the flow around a square cylinder without a plate at Reynolds number 150

Sect. 4, it was observed that at Reynolds numbers 50 and 52, the flow was not really stable when using a convergence criterion of 10^{-7}, in reality the flow maintained a steady status for about 13 s, and slowly became transient with a very small amplitude and frequency. When employing this smaller convergence criterion, and allowing the simulations to run for over 17 s, the critical Reynolds number was found to be 48. According to the experimental investigation performed by Sohankar et al. [8], the critical Reynolds number is 47 ± 2, which has a good agreement with the result obtained in the present study.

Besides the square cylinder without the splitter plate, the other two geometries, geometry A and B, studied in the present section are shown in Fig. 6. In both geometries the splitter plate length was 3.0L, for geometry A the distance between the splitter plate and the square cylinder was also 3.0L. In geometry B, the splitter plate was attached to the square cylinder upstream face.

Table 3 introduces the critical Reynolds numbers separating steady from unsteady periodic flows and for the three geometries studied, these values were obtained once the total relative error between two consecutive iterations was kept to 10^{-8}. It is concluded

Fig. 6 Geometries A and B with different distance D^*

Plate

Square cylinder

Square cylinder

Plate

L

L Charcateristic length
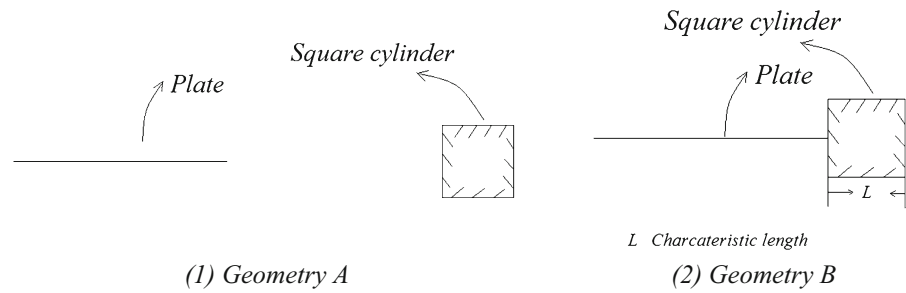
(1) Geometry A

(2) Geometry B

Table 3 The critical Reynolds numbers for the three different geometries studied, distinguishing laminar steady from unsteady flows

Geometry	Square cylinder	A	B
Critical *Re* LBM	48	56	59
Critical *Re* Nektar++	48	56	59

Table 4 Vortex length over the characteristic length for different geometries with different distances between the plate and the square cylinder

Geometry	Square cylinder	A	B
Critical *Re*	47	55	58
L_v/L	3.48710	3.0686	2.9159

that the critical Reynolds number increases as the distance splitter plate-square cylinder decreases from infinite to zero. This conclusion was obtained not only by the in-house LBM code, but also by the open source software *Nektar++*. Although in this paper only three values of the distance were tested, it is believed by the present authors that, the critical Reynolds numbers obtained are defining the upper and lower limits of all possible critical Reynolds numbers, regardless of the upstream splitter plate position and providing the splitter plate length is maintained constant at 3.0L. The plate thickness was negligible, $Tk^* = 0.0L$. Notice that it is the first time this particular splitter plate location is considered. Regarding the comparisons presented in Table 3, it is interesting to highlight that the computational time consumed when *Nektar++* was used, was about 1/10 of the time required by the LBM simulations.

Table 4 introduces the length of the steady trailing vortex L_v over the characteristic length of the edge L and for the three geometries studied in this section. For each geometry, the largest Reynolds number at which the flow remains steady is presented. It can be seen, that the length of the downstream laminar bubble decreases as the splitter plate is displaced towards the square cylinder, as clarified before under these conditions the critical Reynolds number increases.

Figure 7 presents the streamlines and the pressure contour lines, left hand side and right hand side of the

figure, respectively, at the largest Reynolds number for each geometry at which the flow is steady. The boundary layer, the mixing layer and the wake, can be clearly differentiated in these figures. Notice for example that the mixing layer does not exist for the cases without the plate and with the plate attached to the square cylinder. The mixing layer will become much more relevant whenever the cases considering an upstream velocity ratio will be evaluated. Regarding the pressure contour lines, it is observed that the use of a splitter plate, regardless of its position, tends to reduce the pressure on the square cylinder upstream face, the pressure acting on the downstream face, suffers a negligible increase as the plate is moved downstream. Based on this results and providing the Reynolds number would remain constant, it could be estimated that the overall drag force on the square cylinder decreases as the splitter plate moves downstream. In the cases presented in Fig. 7, the Reynolds numbers are different, the critical Reynolds numbers increase as the plate is moved downstream, yet and due to fact that the Reynolds number increase is small, the force acting on the square cylinder front face slightly decreases as the plate displaces towards the cylinder. Such non-dimensional force is 0.1129975 for the square cylinder, 0.112251 for configuration A, and 0.111821 for configuration B, the respective forces on the downstream vertical wall were 0.1104375, 0.1105775 and 0.1105545. In other words, as the plate

moves towards the cylinder, the forces acting on the square cylinder decrease, even though the critical Reynolds numbers characterizing the three geometries presented in Fig. 7 are different.

5.2 Evaluation of the velocity ratio (r^*) effect on the flow field

This section is devoted to study the velocity ratio effect on the flow field. All simulations were carried out by using LBM. The parameters remaining constant were, the upstream length $D^* = 3.0L$, and the splitter plate thickness $Tk^* = 0.0L$. Figure 8 presents the average drag coefficient and the non-dimensional frequency as a function of the velocity ratio and for five slightly different Reynolds numbers, defined based on the velocity below the plate. It is observed that, regardless of the Reynolds number employed, both parameters increase with the velocity ratio increase. As the velocity ratio increases, the boundary layer temporal average thickness ε, on the square cylinder upper horizontal surface keeps decreasing. The equation characterizing such decrease at Reynolds number 52, measured at the center of the upper horizontal surface, reads as follows
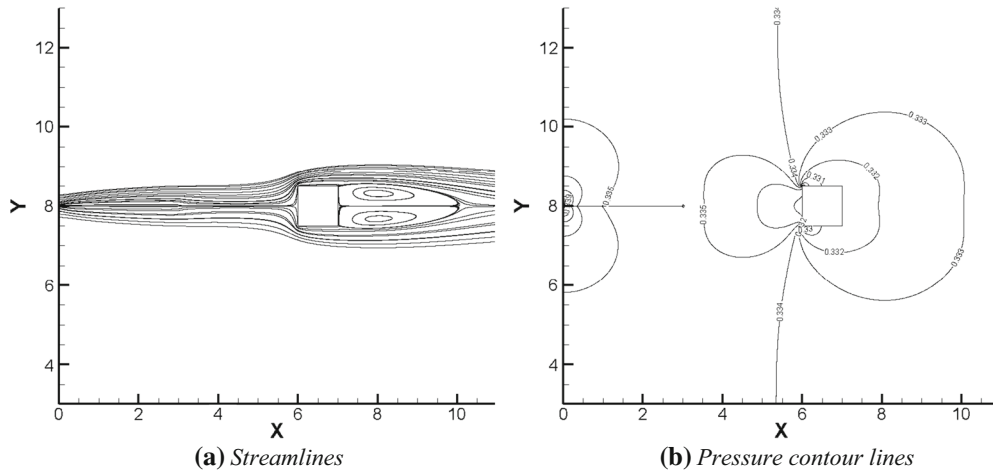
$$\varepsilon = -0.015(r^*)^3 + 0.1414(r^*)^2 - 0.5375r^* + 1.1511 \tag{18}$$

A decrease of the flapping layer thickness has associated an increase of the flapping layer stiffness, the flapping amplitude keeps decreasing, and as a result, the frequency associated to the flapping layer fluctuation increases. This is the explanation of the non-dimensional frequency increase observed in Fig. 8(2). In the same figure, it is observed that for velocity ratios higher than 3.0, the curves at different Reynolds numbers, tend to separate from each other. The authors believe, this phenomenon is associated to the onset of the three dimensional structures appearing in the fluid, notice that at higher Reynolds numbers, the curves further separate from the rest. The evolution of the drag coefficient as a function of the velocity ratio, Fig. 8(1), shows no appreciable difference, between the different Reynolds numbers, at any of the velocity ratios evaluated. The initial appearance of the three dimensional structures do not seem to have a relevant effect on the drag coefficient.
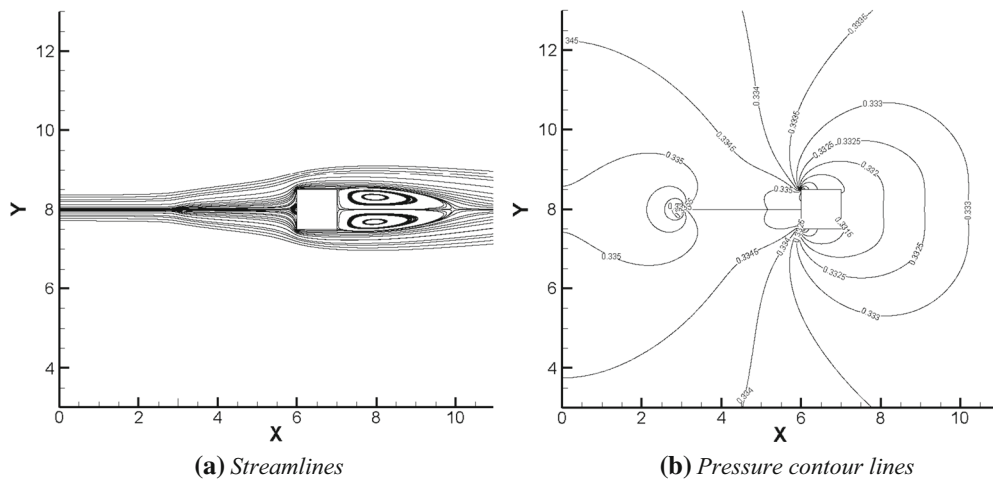
In order to further understand the effects the velocity ratio is causing on the vortex shedding and boundary layer thickness, the vorticity contours for a given Reynolds number 52 and a given time $t = 1.7414$ s are introduced in Fig. 9(1). Four different velocity ratios are compared. Whenever the velocity ratio is 1.0, the flow is steady, as observed in Fig. 9 (1-a) as well as in Fig. 7. Under these conditions, a steady laminar bubble appears downstream of the square cylinder. For velocity ratios 2.0 and 3.0, see Figs. 9(1-b) and 9 (1-c), the downstream vortex shedding is controlled by Kelvin–Helmholtz instabilities. Notice that the boundary layer acting on the square cylinder lower horizontal surface, generates a very low-intensity vorticity which dissipates downstream, the negative vortex generated on the square cylinder upper horizontal surface, takes control of the flow. A much richer downstream vortex generation is observed for a velocity ratio 4.0, see Fig. 9(1-d). Under these conditions, vortex shedding is generated from both, upper and lower, square cylinder horizontal surfaces. The negative vortex generated on the upper surface, has the maximum intensity associated and it will dominate the downstream vortex shedding. From the square cylinder lower surface, a pair of positive and negative vortices are coupled together, their respective origin is, the flapping of the boundary layer appearing at the square cylinder lower surface, and the flow interaction at the mixing layer, just before the square cylinder front face. The Fourier transformation of the dynamic drag forces acting on the square cylinder, clearly shows two main non-dimensional frequencies, the dominant one $f_1 = 0.1699$ is associated to the main vortex generated on the upper surface, and it is due to the boundary layer flapping. This is the only frequency reported in Figs. 8(2) and 10(2) for velocity ratio $r^* = 4.0$. The secondary frequency $f_2 = 0.24272$, is associated to the low intensity positive vortices, generated due to the boundary layer flapping at the square cylinder bottom surface. In fact, a second phenomenon, which is associated to the fluid entrainment at the mixing layer existing between the splitter plate and the square cylinder front face, is generating small intensity negative vortices, which couple with the positive vortices created below the cylinder. This pair of coupled vortices dissipate downstream, leaving a typical Kelvin–Helmholtz vortex shedding flow as the remaining one. Notice that under these conditions, the flow is quasi-periodic. All the process just

(a) *Streamlines* **(b)** *Pressure contour lines*
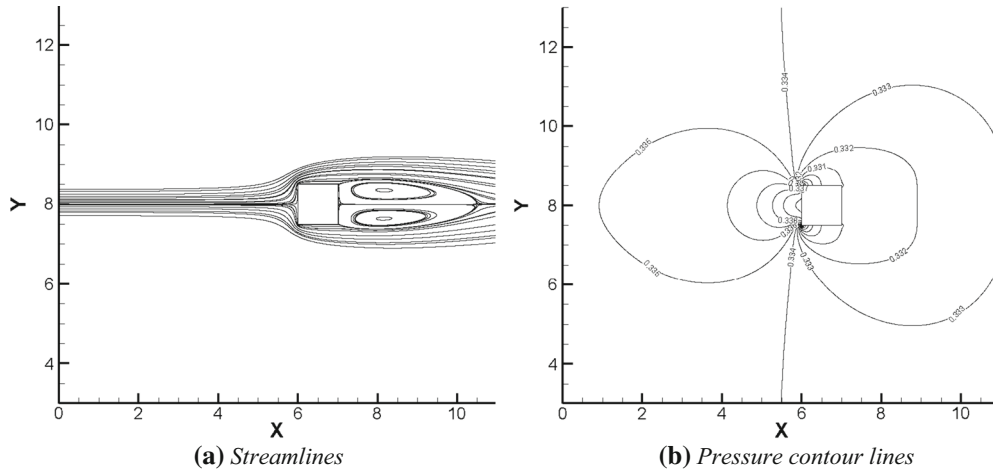
(1) Square cylinder without splitter plate at Re=47

(a) *Streamlines* **(b)** *Pressure contour lines*

(2) Geometry A, $D^* = 3.0L$, $r^* = 1.0$, $Tk^* = 0.0L$ at Re=55

(a) *Streamlines* **(b)** *Pressure contour lines*

(3) Geometry B, $D^* = 0.0L$, $r^* = 1.0$, $Tk^* = 0.0L$ at Re=58

◄ **Fig. 7** Streamlines at the largest steady Reynolds numbers of three geometries (Square cylinder, geometries A and B) in the present study. (1) Square cylinder without splitter plate, $Re = 47$. (2) Geometry A, $D^* = 3.0L$, $Tk^* = 0.0L$, $Re = 55$. (3) Geometry B, $D^* = 0.0L$, $Tk^* = 0.0L$, $Re = 58$. For all cases the velocity ratio $r^* = 1.0$

explained, can be more clearly seen in Fig. 9(2), where the fluid entrainment at the mixing layer is more clearly observed. As a matter of a fact, in Fig. 9(2) at time steps $t1 = 1.7362$ s and $t2 = 1.7388$ s, it is observed that a small negative vortex is generated at the mixing layer, and it is transported downstream merging/coupling with the positive vortices generated below the square cylinder, which dissipate downstream. It is interesting to highlight that, under these conditions, the vortices generated in the mixing layer are always negative, and always merge with the positive vortices appearing below the cylinder.

In order to further evaluate the effect of the distance between splitter plate and square cylinder front face, D^*, at Reynolds number 52 Fig. 10 was generated. For each of the velocity ratios considered, four different distances from $1.0L$ to $4.0L$ were studied. Based on the results presented in Fig. 10, it can be stated that the dominant parameter conducting the flow dynamics, is the velocity ratio. Then, neither the drag coefficient nor the non-dimensional frequency, appeared to be much affected by the distance D^*. Based on what can be observed in Fig. 10(2), it seems at low velocity ratios, the distance D^* shows some relevance on the final vortex shedding frequency, small distances tend to generate a slightly higher frequency.

5.3 Evaluation of the effect of different plate thicknesses on the flow characteristics

In this section some flow properties when changing the plate thickness Tk^*, were investigated by using LBM. Four thicknesses, $Tk^* = 0.0L$, $0.1L$, $0.2L$ and $0.3L$, were considered. The parameters remaining constant were, the upstream length $D^* = 3L$ and the velocity ratio $r^* = 1.0$.

Table 5 compares, for three different Reynolds numbers, 100, 120 and 150, the average drag coefficient and the non-dimensional frequencies as a function of the four values of the plate thickness. From this table, it can be observed that for the Reynolds numbers 100 and 120, the mean value of the drag coefficient, increases as the plate thickness increases. At Reynolds number 150, the mean value of the drag coefficient has an initial decrease and whenever the plate thickness is $0.2L$ or higher, it increases. This effect is explained whenever the average pressure at the upstream/downstream vertical walls is studied. At Reynolds numbers 100 and 120, when the plate thickness increases from $0.0L$ to $0.3L$, the average non-dimensional pressure at the leading face increases respectively by 0.19% and 0.11%, while the average non-dimensional pressure at the trailing vertical wall decreases respectively by 0.268% and 0.249%. For these two Reynolds numbers at which the flow is mostly periodic, the increase of drag coefficient is mostly affected by the decrease of the downstream non-dimensional pressure. At Reynolds number 150, for a plate thickness of $0.0L$, the flow is periodic and becomes quasi-periodic as the plate thickness increases to $0.1L$. This particular change of the flow
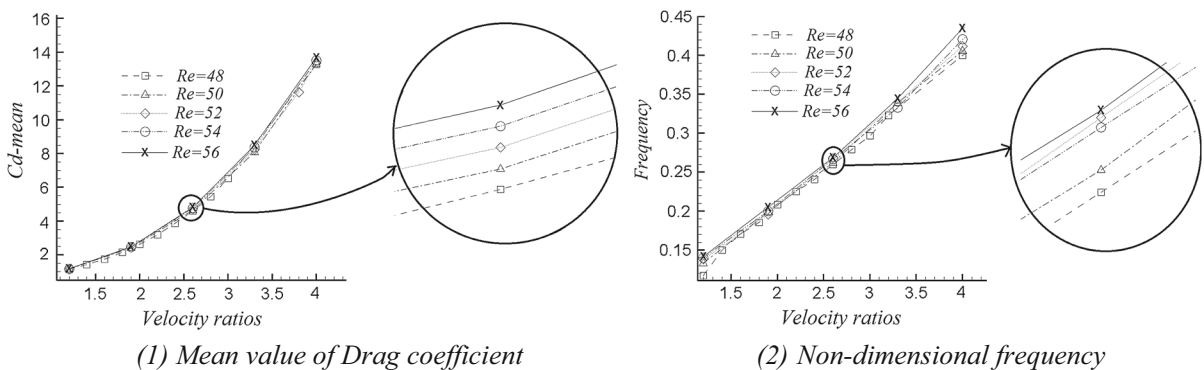

(1) Mean value of Drag coefficient

(2) Non-dimensional frequency

Fig. 8 The mean value of drag coefficient and the non-dimensional frequency versus the parameter r^* at Reynolds number from 48 to 56
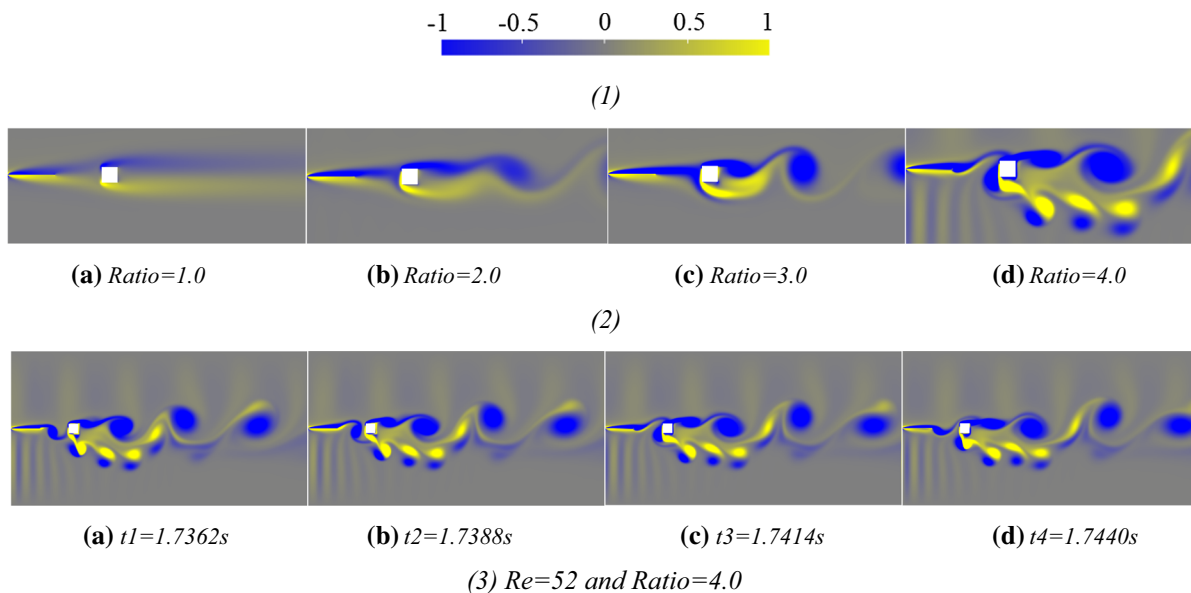
Fig. 9 (1) Vorticity contours reference bar. (2) Vortex shedding process at a given time with four different velocity ratios at $Re = 52$. (3) Vortex shedding process at four different time steps with velocity ratio $r^* = 4.0$ at $Re = 52$. In both figures, the plate thickness is null, $Tk^* = 0.0L$

structure, generates a decrease of the average non-dimensional pressure at the front face of 0.2%, generating as well a small decrease at the downstream vertical wall average non-dimensional pressure of 0.036%. As the plate thickness keeps increasing, the percentage decrease of the average non-dimensional pressure at the front face, tends to zero, while the percentage decrease at the downstream face, increases sharply, therefore clarifying why the average drag coefficient increases. Notice from Fig. 12 (2), that for a plate thickness of 0.3L, two alternative vortices, positive and negative, appear at the mixing layer. These vortices, once coupled with the square cylinder upper and lower boundary layers, they decisively affect the downstream non-dimensional pressure, decreasing it further. As a general trend, it can be said that the downstream average pressure tends to decrease as the plate thickness increases.

For a given plate thickness, as Reynolds number increases from 100 to 150, the average value of drag coefficient decreases. This happens for all plate thicknesses. The physical explanation of why is this happening, is again to be found when checking the pressure on the upstream/downstream surfaces. For any given plate thickness as Reynolds number increases, the pressure at the front and rear faces increases, but the percentage increase of the non-

dimensional pressure at the rear face, is always higher than the one at the front face, explaining why the drag coefficient decreases. As an example, it can stated that for plate thickness of 0.0L, when the Reynolds number goes from 100 to 150, the front face average non-dimensional pressure increases by 0.228%, while the average non-dimensional pressure at the rear face increases by 0.26%. For the case of an isolated square cylinder, the decrease of the drag coefficient when the Reynolds number increases, was previously reported by other scholars [6, 7, 13, 18, 27–29]. See for example Table 3 in reference 1, figure 3 in reference 2, figure 3 in reference 3, figure 4(a) in reference 4, figure10(a) inference 5, Table 1 in reference 6 and Table 2 in reference 7. When considering the drag coefficient amplitude, it is observed, it increases sharply as the plate thickness increases, clearly indicating that under these conditions, the boundary layer thickness increases. For a given plate thickness, as the Reynolds number increases, the drag coefficient amplitude slightly increases. This is explained when observing the coupling effect of the mixing layer with the boundary layers located on the top and bottom surfaces of the square cylinder. As Reynolds number increases, the mixing layer upstream of the square cylinder is further enhanced, and the alternative coupling between the mixing and boundary layers,
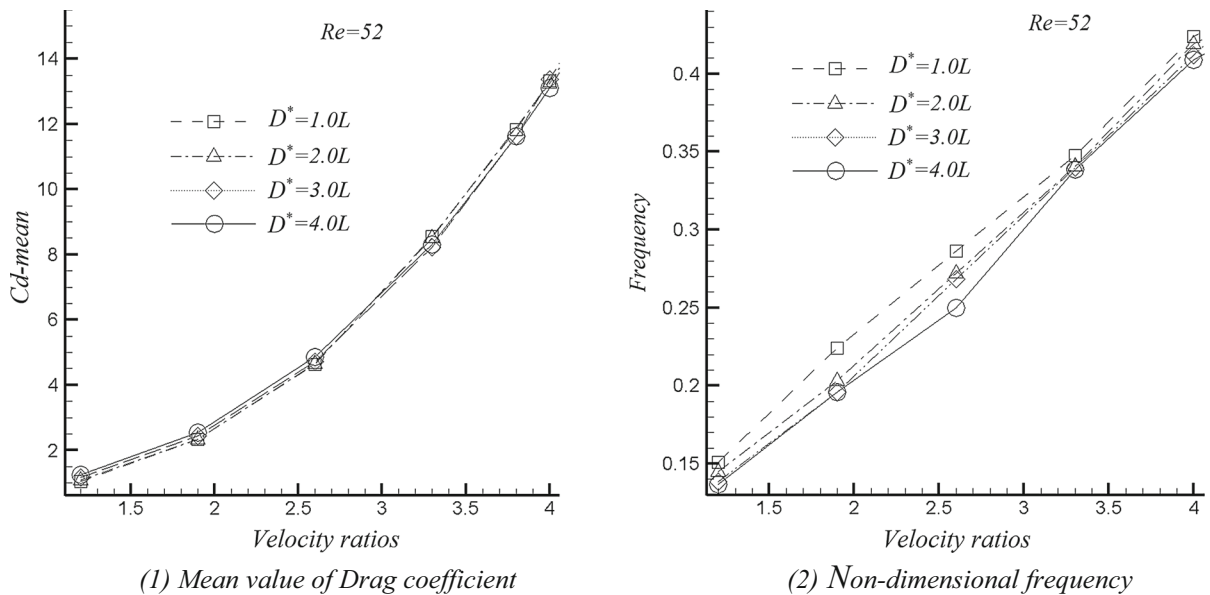
Fig. 10 Mean value of the drag coefficient and the non-dimensional frequency versus the velocity ratio r^*, as a function of four different splitter plate square cylinder distances, from 1.0L to 4.0L. Reynolds number 52

brings a small increase on the boundary layer flapping amplitude. Regarding the non-dimensional frequency, at Reynolds number 100, it slightly increases as the plate thickness increases. Notice that whenever the plate thickness is 0.3L, the flow becomes quasi-periodic, therefore two main frequencies characterize the flow fluctuations. The main frequency is associated to the square cylinder downstream vortex shedding, while the secondary frequency is originated at the mixing layer. The quasi-periodicity of the flow, is observed at smaller plate thicknesses when Reynolds number increases.

Figure 11 represents characteristic periodic and quasi-periodic stages of the flow. Each plot is divided into two sub-plots, the inset represents the time series of the drag coefficient, and the main panel introduces the Fourier transformation obtained from this time signal. A typical periodic solution, for $Re = 100$ and $Tk^* = 0.0L$ is presented in Fig. 11(1). Notice that a single frequency is observed in the main panel. In Fig. 11(2), one of the quasi-periodic solutions, defined by $Re = 150$, $Tk^* = 0.3L$, is introduced, where the two characteristic frequencies are observed.

In order to visualize the coupling between the mixing and boundary layers, Fig. 12 was generated. In this figure and for a Reynolds number 150, several snapshots taken at different time steps, are compared

for two plate thicknesses 0.0L and 0.3L. The first thing which is observed is that in both cases, the flow is controlled by the Von Karman vortex shedding. When observing the snapshots presented in Fig. 12(1), it is seen that the mixing layer appearing before the square cylinder, it is very thin and suffers an alternative flapping. Whenever the mixing layer reaches the square cylinder front face, it merges/couples alternatively with the boundary layers located on the top and bottom surface of the square cylinder. As the plate thickness increases to 0.3L, see Fig. 12(2), the mixing layer is further enhanced, being now capable of generating alternative positive and negative vortices just before the square cylinder front face. Whenever the low intensity alternative vortices generated by the mixing layer reach the square cylinder front face, if they are negative, they merge/couple with the square cylinder bottom boundary layer, from which the Von Karman positive vortices are generated. On then other hand, the mixing layer negative vortices merge/couple with the square cylinder top boundary layer, generating the Von Karman negative vortices.

The effect on vortex shedding when modifying the Reynolds number, is introduced in Fig. 13. When comparing the snapshots introduced in Fig. 13(1) and (2), it is observed, that as Reynolds number increases, the flow entrainment existing on the mixing layer is

Table 5 Flow parameters for different geometries with different thickness at Reynolds numbers 100, 120 and 150

Re thickness	0.0L	0.1L	0.2L	0.3L
100				
$Cd - mean$	1.98145	2.01554	2.07416	2.15264
$Cd - amp$	0.1903	0.2069	0.24625	0.4325
Frequency	$f = 0.34794$	$f = 0.34897$	$f = 0.34995$	$f_1 = 0.35$
				$f_2 = 0.6285$
Re thickness	0.0L	0.1L	0.2L	0.3L
120				
$Cd - mean$	1.92409	1.97099	2.03013	2.11732
$Cd - amp$	0.1983	0.20245	0.24775	0.4375
Frequency	$f = 0.34889$	$f = 0.35$	$f_1 = 0.35044$	$f_1 = 0.35$
			$f_2 = 0.6301$	$f_2 = 0.63201$
Re thickness	0.0L	0.1L	0.2L	0.3L
150				
$Cd - mean$	1.95524	1.84719	1.93105	1.98879
$Cd - amp$	0.2061	0.2172	0.3197	0.44625
Frequency	$f = 0.34909$	$f_1 = 0.351111$	$f_1 = 0.3512$	$f_1 = 0.352$
		$f_2 = 0.6311$	$f_2 = 0.632$	$f_2 = 0.63321$

more intense. Notice from Fig. 13(2), that alternative positive and negative vortices appear upstream of the square cylinder. Due to the weaker mixing layer appearing at Reynolds number 100, see Fig. 13(1), this upstream alternative vortices do not appear. In any case, regardless of the existence of upstream vortices, the mixing layer couples alternatively with the boundary layers appearing on the square cylinder top and bottom surfaces, generating the typical downstream Von Karman vortex shedding. As a conclusion, a similar effect appears when increasing the splitter plate thickness or the Reynolds number, in both cases alternative positive and negative vortices are generated on the mixing layer upstream of the square cylinder. Although, the ones generated when the plate thickness is increased, are more clearly delimited.

5.4 Applications of the POD method

In this subsection, initially a set of tables defining the different cases (data blocks) simulated by LBM are introduced. By using the POD method based on the information gathered from the different data blocks, predicted results were obtained for three different modified parameters (three aiming blocks). In subsection 5.4.1, the aiming mode regarding the parameter D^*, was predicted by using the POD method based on the information gathered from the existing data blocks defined in Tables 6 and 7, while in Subsections 5.4.2 and 5.4.3, the same procedure was performed to evaluate unsteady cases with changeable parameters r^* and Tk^* respectively.

5.4.1 Application of the POD method for steady cases and for different distances between splitter plate and square cylinder, D^*

In this section, the parameters which remained constant and their respective values were $r^* = 1.0$ and $Tk^* = 0.0L$. The range of Reynolds numbers evaluated fall between 5 and 30. Initially, a set of new cases defined in Tables 6 and 7, were simulated using LBM, and the pressure fields obtained were gathered to build the sample matrix required for the POD method. Once the sample matrix was obtained, it was used to predict the pressure fields at different cases not previously studied. In order to validate the new results, the pressure fields predicted by using the POD method were compared with the ones simulated with LBM and for the same conditions.
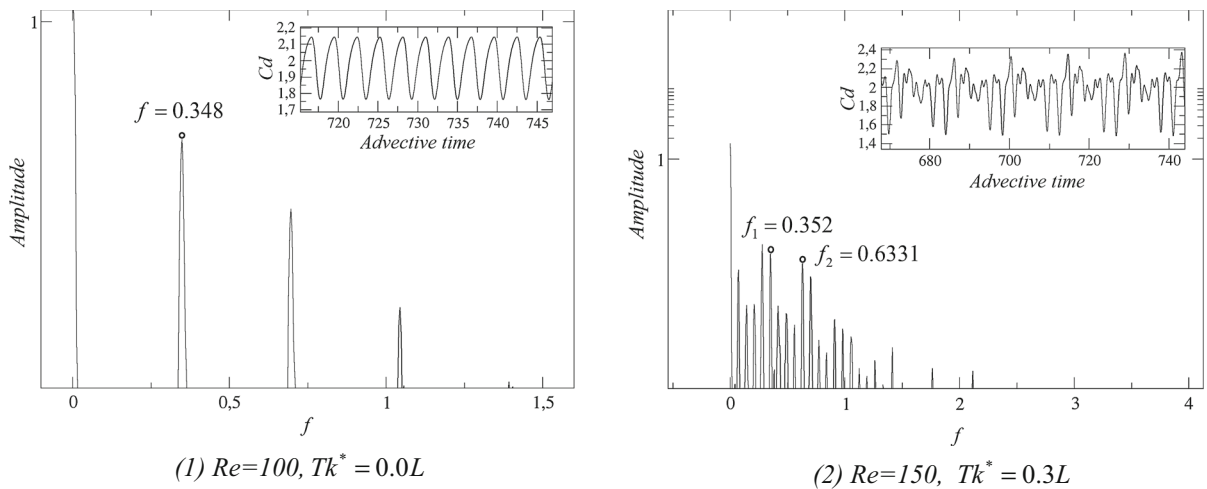
(1) Re=100, Tk* = 0.0L

(2) Re=150, Tk* = 0.3L

Fig. 11 (1) *Re* = 100, *Tk** = 0.0*L*, the periodic signal of the time series of drag coefficient. (2) *Re* = 150, *Tk** = 0.3*L*, the quasi-periodic orbit of the time series of drag coefficient
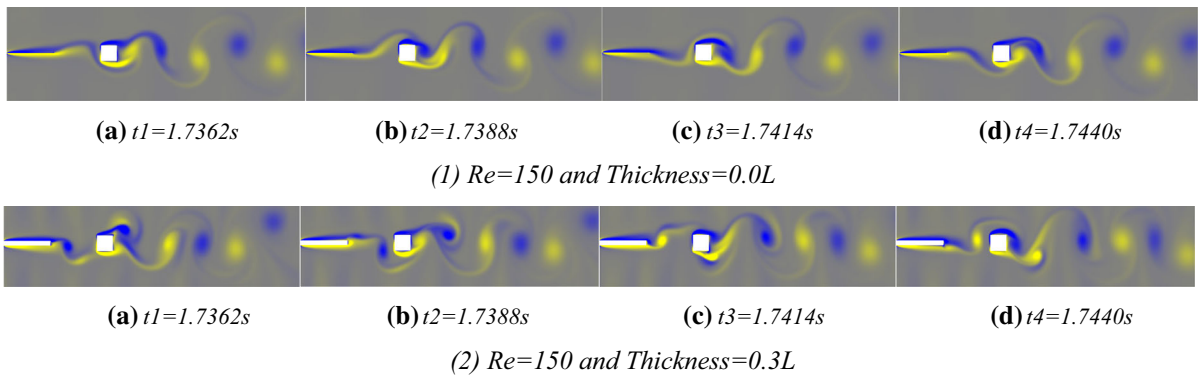

(a) *t1=1.7362s*   **(b)** *t2=1.7388s*   **(c)** *t3=1.7414s*   **(d)** *t4=1.7440s*

(1) Re=150 and Thickness=0.0L

(a) *t1=1.7362s*   **(b)** *t2=1.7388s*   **(c)** *t3=1.7414s*   **(d)** *t4=1.7440s*

(2) Re=150 and Thickness=0.3L

Fig. 12 Introduces the vortex shedding process for a given Reynolds number 150, at two plate thicknesses. (1) *Tk** = 0.0*L*. (2)*Tk** = 0.3*L*

The classic snapshot POD method presented by Sirovich [21] was employed in the present study. The computational approach followed in the present work is concluded in the following steps.

1. Obtaining the sample matrix based on *M* existing results (data blocks), each data block contains *N* snapshots.
2. Solving the eigenvalues and eigenvectors of the correlated matrix obtained by Eq. (10).
3. Constructing the base vectors with the eigenvalues and eigenvectors by Eq. (11).
4. Calculating the empirical coefficients by Eq. (12).
5. Computing the target empirical coefficients based on the empirical coefficients of existing data blocks by 2D bi-cubic spline interpolation.

6. Reconstructing the aiming block (data block) with the obtained target empirical coefficients by Eq. (13).

In Fig. 14(1), the pressure contour lines around the square cylinder, for *Re* = 20, plate thickness *Tk** = 0.0*L* and plate square distance *D** = 2.0*L*, obtained from the POD prediction, are compared with the ones simulated using LBM. For this particular POD prediction, all the cases introduced in Table 6 were initially simulated using LBM, the pressure fields from these cases were employed to generate the sample matrix. Notice that just 12 cases (data blocks) were used to generate the POD sample matrix. Due to the fact, that few data blocks were employed for the POD prediction, some clear differences can be observed
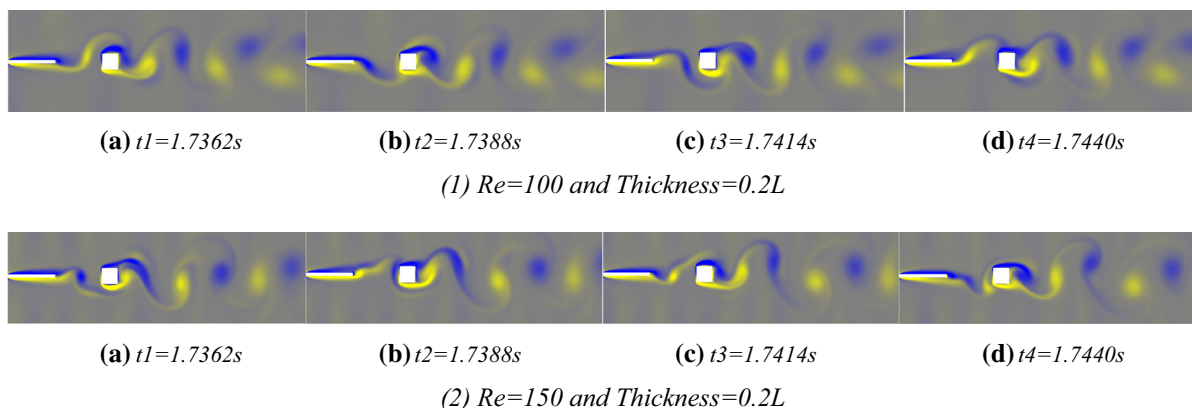
(a) *t1=1.7362s*   **(b)** *t2=1.7388s*   **(c)** *t3=1.7414s*   **(d)** *t4=1.7440s*

(1) Re=100 and Thickness=0.2L

(a) *t1=1.7362s*   **(b)** *t2=1.7388s*   **(c)** *t3=1.7414s*   **(d)** *t4=1.7440s*

(2) Re=150 and Thickness=0.2L

Fig. 13 Introduces the vortex shedding process for given plate thickness $Tk^* = 0.2L$ at two Reynolds numbers. (1) *Re = 100.* (2) *Re = 150*

between the predicted and simulated results. In Fig. 14(2), the same predicted and simulated results are presented, for this particular case a total of 35 data blocks, introduced in Table 7, were used to create the POD sample matrix. Clearly when the number of the data blocks increases, the predicted results gain in accuracy, this is why in Fig. 14(2), both predicted and simulated results are almost identical.

5.4.2 Application of the POD method for unsteady cases and for different velocity ratios, r^*

For the present section, the parameters which were kept constant are, the plate thickness $Tk^* = 0.0L$ and the distance between splitter plate and the square cylinder $D^* = 3.0L$. As the flow is meant to be unsteady, the Reynolds numbers range evaluated goes from 48 to 56. For each of the different Reynolds numbers, several velocity ratios ranging from 1.2 to 4.0 were considered. As in the previous case, two different number of data blocks, introduced in Tables 8 and 9, were employed. Each table characterizes the LBM simulations performed to obtain the information required to build the sample matrix. Two sample matrices were built, one based on the

simulations described in Table 8 and the second one based on the simulations described in Table 9. Using each sample matrix and following the steps described in Sect. 5.4.1, two POD predictions were performed.

In order to compare the results obtained from the predictions and the simulations, a new case at Reynolds number 53 and velocity ratio 3.1, is defined in Table 10 and Fig. 15. Three variables were used for comparison in Table 10, the drag coefficient average value, amplitude and the non-dimensional frequency. When the prediction was done using the 9 data blocks sample matrix introduced in Table 8, some clear differences are observed when comparing with the results obtained via using LBM. As the number of data blocks increased to 25, see Table 9, the precision sharply increased, yet it appears that 25 data blocks sample matrix might still not be sufficient to obtain very accurate results. In order to further analyze the dynamic results, Fig. 15 was presented. In this figure, it is introduced the temporal value of the drag coefficient obtained using LBM and the POD predictions with 9 and 25 data blocks. Under the macroscopic point of view, all three results are very similar, although the zoomed view clarifies that the prediction obtained using 9 data blocks clearly differ from the

Table 6 Different LBM simulated cases (12 data blocks) used for POD prediction for different plate square distances

Existing data blocks	No. 1	No. 2	No. 3	No. 4	No. 5	No. 6	No. 7	No. 8	No. 9	No. 10	No. 11	No. 12
Re	10	10	10	15	15	15	25	25	25	30	30	30
D^*	1.0L	2.0L	3.0L	1.0L	2.0L	3.0L	1.0L	2.0L	3.0L	1.0L	2.0L	3.0L

Table 7 Different LBM simulated cases (35 data blocks) used for POD prediction for different plate square distances

Existing data blocks	No. 1	No. 2	No. 3	No. 4	No. 5	No. 6	No. 7	No. 8	No. 9	No. 10	No. 11	No. 12	No. 13	No. 14	No. 15	No. 16	No. 17	No. 18
Re	5	5	5	5	5	5	5	10	10	10	10	10	10	10	15	15	15	15
D^*	0.0L	0.5L	1.0L	1.5L	2.0L	2.5L	3.0L	0.0L	0.5L	1.0L	1.5L	2.0L	2.5L	3.0L	0.0L	0.5L	1.0L	1.5L

Existing data blocks	No. 19	No. 20	No. 21	No. 22	No. 23	No. 24	No. 25	No. 26	No. 27	No. 28	No. 29	No. 30	No. 31	No. 32	No. 33	No. 34	No. 35
Re	15	15	15	25	25	25	25	25	25	25	30	30	30	30	30	30	30
D^*	2.0L	2.5L	3.0L	0.0L	0.5L	1.0L	1.5L	2.0L	2.5L	3.0L	0.0L	0.5L	1.0L	1.5L	2.0L	2.5L	3.0L

LBM simulation, once 25 data blocks are employed, the agreement is much closer. In any case, and in order to further increase the agreement with the dynamic results, a higher number of data blocks should be employed.

5.4.3 Application of the POD method for unsteady cases and for different plate thicknesses Tk^*

For the present section, the parameters being kept constant are, the velocity ratio $r^* = 1.0$ and the distance between splitter plate and the square cylinder $D^* = 3.0L$.

Three different Reynolds numbers 100, 120 and 150, as well as four different plate thicknesses, were considered. A total number of 12 cases (data blocks) were initially simulated using LBM. The flow dynamics behind these cases were already presented Sect. 5.3 (Table 11).

As in the previous section, to analyze the results, a table and a figure were generated. Table 12 compares the results obtained from the LBM simulation and the POD prediction at Reynolds number 125 and plate thickness $Tk^* = 0.0L$. Three variables, the drag coefficient average value, amplitude and the non-dimensional frequency were evaluated. The comparison of the predicted drag coefficient obtained by POD with the simulated one performed with LBM was good, the drag coefficient average value, amplitude and the non-dimensional frequency were in good agreement. The dynamic results are presented in Fig. 16, from where it is observed that the predicted drag coefficient amplitude exceeds by 9 percent the one obtained from the LBM simulation. On the other hand, the oscillation frequency is exactly the same. As already observed in the previous section, an increase of the number of the data blocks would improve the results accuracy. Notice that the results obtained from the POD prediction are in phase and amplitude slightly different than the simulated ones obtained via using LB. It is believed by the present authors that due to the limited number of the data blocks employed, the POD prediction in the present study is not extremely accurate. Besides, the sample matrix is obtained using stable signals, the transient parts were eliminated at the very beginning, which may lead to a signal delay in the POD prediction.
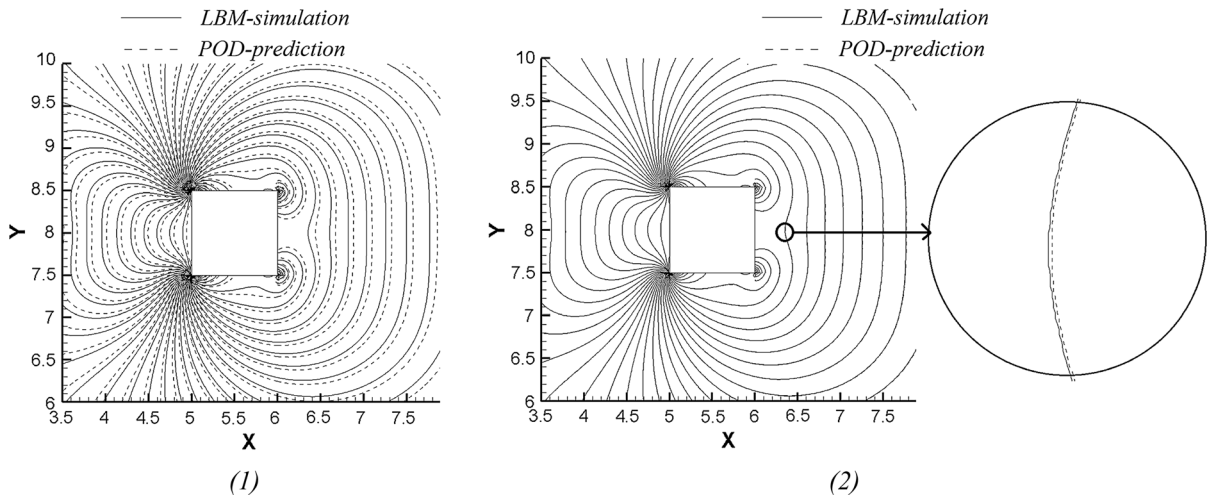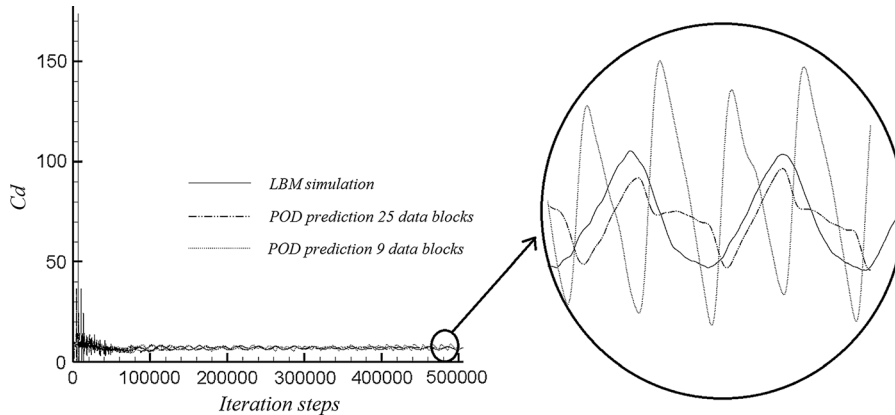
Fig. 14 Pressure contour lines compared between LBM simulation and POD prediction (12 and 35 data blocks), at Reynolds number 20 with $D^* = 2.0L$ and $Tk^* = 0.0L$

Table 8 Different LBM simulated cases (9 data blocks) used for POD prediction for different velocity ratios

Existing data blocks	No. 1	No. 2	No. 3	No. 4	No. 5	No. 6	No. 7	No. 8	No. 9
Re	48	48	48	52	52	52	56	56	56
r^*	1.2	2.6	4.0	1.2	2.6	4.0	1.2	2.6	4.0

Table 9 Different LBM simulated cases (25 data blocks) used for POD prediction for different velocity ratios

Existing data blocks	No. 1	No. 2	No. 3	No. 4	No. 5	No. 6	No. 7	No. 8	No. 9	No. 10	No. 11	No. 12	No. 13
Re	48	48	48	48	48	50	50	50	50	50	52	52	52
r^*	1.2	1.9	2.6	3.3	4.0	1.2	1.9	2.6	3.3	4.0	1.2	1.9	2.6
Existing data blocks	No. 14	No. 15	No. 16	No. 17	No. 18	No. 19	No. 20	No. 21	No. 22	No. 23	No. 24	No. 25	
Re	52	52	54	54	54	54	54	56	56	56	56	56	
r^*	3.3	4.0	1.2	1.9	2.6	3.3	4.0	1.2	1.9	2.6	3.3	4.0	

6 Conclusions

In the present work, a numerical investigation of passive flow control over a square cylinder was performed through three changeable parameters, the velocity ratio, the plate thickness and the distance between the plate and the square cylinder, different laminar Reynolds numbers were considered. It is concluded that

- For a given velocity ratio $r^* = 1.0$ and a given plate thickness $Tk^* = 0.0L$, the distance D^* affects

the critical value of the Hopf bifurcation, which separate the steady and unsteady periodic flows. From the study of three values of the parameter D^*, infinite, $3.0L$ and $0.0L$, it is obtained that the respective critical values are 48, 56 and 59.

- For a given distance $D^* = 3.0L$ and a given plate thickness $Tk^* = 0.0L$, the parameter velocity ratio r^* ranging from 1.2 to 4.0 was studied. The tested Reynolds numbers varied from 48 to 56. For a given Reynolds number, the drag coefficient mean value and the non-dimensional frequency increase

Table 10 Three variables obtained from the LBM simulation and POD predictions

Aiming block	Parameters	LBM simulation	POD 9 data blocks	POD 25 data blocks
$Re = 53$	$Cd - mean$	7.10937	7.20294	7.14396
$r^* = 3.1$	$Cd - amp$	0.81088	1.92009	0.76099
	f	0.3256	0.339	0.3296

Fig. 15 Pressure contour lines compared between LBM simulation and POD prediction (9 and 25 data blocks), at Reynolds number 53 with $r^* = 3.1$

Table 11 Different LBM simulated cases (12 data blocks) used for POD prediction for different plate thicknesses

Existing data blocks	No. 1	No. 2	No. 3	No. 4	No. 5	No. 6	No. 7	No. 8	No. 9	No. 10	No. 11	No. 12
Re	100	100	100	100	120	120	120	120	150	150	150	150
Tk^*	0.0L	0.1L	0.2L	0.3L	0.0L	0.1L	0.2L	0.3L	0.0L	0.1L	0.2L	0.3L

as the velocity ratio increases. For a given velocity ratio, the drag coefficient mean value and the non-dimensional frequency slightly increase as the Reynolds number increases. It is found that the mixing layer was dramatically affected by this parameter r^*, the mixing layer interacts with the boundary layer flapping at the top and bottom of the square cylinder, changing the downstream vortex shedding from Von Karman to Kelvin–Helmholtz.

- For a given distance $D^* = 3.0L$, a given plate thickness $Tk^* = 0.0L$ and a given Reynolds number 52, the effect of the velocity ratio r^* versus the distance D^* was analyzed. It is found that, compared with the plate square distance D^*, the velocity ratio r^* plays a more important role to modify the flow structure, due to its effect on the mixing layer upstream of the square cylinder.

- For a given velocity ratio $r^* = 1.0$ and a given distance $D^* = 3.0L$, the thickness Tk^* brought forward the appearance of the Neimark–Sacker bifurcation, which defines the border between unsteady periodic and quasi-periodic flows. It is observed that, for a given thickness, the drag coefficient mean value decreases as the Reynolds number increases. Yet, for a given Reynolds number, the drag coefficient mean value increases as the thickness increases.

- From the POD predictions, it is concluded that based on a sample matrix with limited data blocks, the POD method is a very appropriate tool reduce the computational costs via using the existing data.

Table 12 Three variables obtained from the LBM simulation and POD prediction

Aiming block	Parameters	LBM simulation	POD 12 data blocks
Re = 125	Cd − mean	1.8755	1.9275
Tk* = 0.0L	Cd − amp	0.2796	0.3075
	f	0.35	0.3498
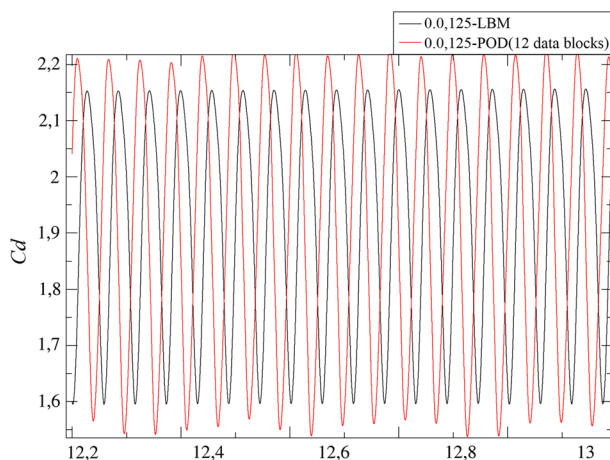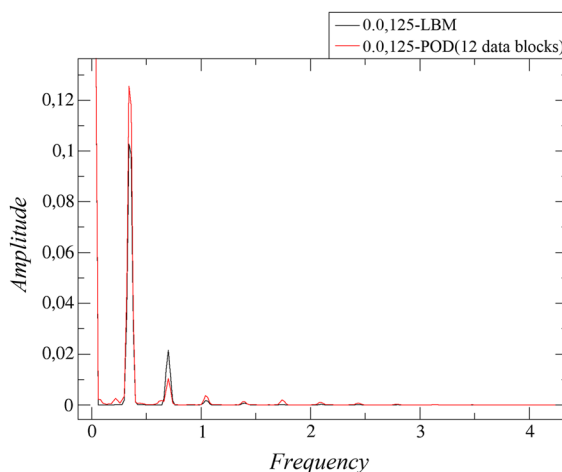
(1) Time series of drag coefficient   *(2) Fourier transformation of Cd*

Fig. 16 (1) Time series of drag coefficient obtained LBM and POD. (2) The Fourier transformation of the signals presented in Fig. 16(1)

- In order to have a trustable prediction, the aiming mode should be falling in the sample matrix range.

Compliance with ethical standards

References

1. Tritton DJ (1959) Experiments on the flow past a circular cylinder at low reynolds numbers. J Fluid Mech 6(04):547–567
2. Braza M, Chassaing P, Ha Minh H (1986) Numerical study and physical analysis of the pressure and velocity fields in the near wake of a circular cylinder. J Fluid Mech 165:79–130
3. Allicvi A, Bermejo R (2009) Numerical simulation of laminar flow past a circular cylinder. Appl Math Model 33:1228–1247
4. Okajima A (1982) Strouhal numbers of rectangular cylinders. J Fluid Mech 123:379–398
5. Kelkar KM, Patankar SV (1992) Numerical prediction of vortex shedding behind a square cylinder. Int J Numer Methods Fluids 14:327–341
6. Sohankar A, Davison L, Norberg C (1995) Numerical simulation of unsteady flow around a square two-dimensional cylinder. In: Twelfth Australian fluid mechnics conference, The University of Sydney, Australia
7. Sohankar A, Norberg C, Davidson L (1999) Simulation of three-dimensional flow around a square cylinder at moderate Reynolds numbers. Phys Fluids 11(2):288–306
8. Sohankar A, Norberg C, Davidson L (1997) Numerical simulation of unsteady flow around a rectangular two-dimensional cylinder at incidence. J Wind Eng Ind Aero 69:189
9. Luo SC, Tong XH, Khoo BC (2007) Transition phenomena in the wake of a square cylinder. J Fluids Struct 23:227–248
10. Ul-Islam S, Zhou CY (2009) Characteristics of flow past a square cylinder using the lattice Boltzmann method. Inf Technol J 8(8):1094–1114
11. MSM Ali, CJ Doolan, V Wheatley (2009) Grid convergence study for a two-dimensional simulation of flow around a

square cylinder at a low Reynolds number. In: Seventh international conference on CFD in the minerals and process industries CSIRO, Melbourne, Australia, 9–11

12. Sohankar A, Norberg C, Davidson L (1998) Low-Reynolds-number flow around a square cylinder at incidence: study of blockage, onset of vortex shedding and outlet boundary condition. Int J Numer Methods Fluids 26:39–56

13. Zhou L, Cheng M, Hung KC (2005) Suppression of fluid force on a square cylinder by flow control. J Fluids Struct 21:151–167

14. Cheng M, Whyte DS, Lou J (2007) Numerical simulation of flow around a square cylinder in uniform-shear flow. J Fluids Struct 23:207–226

15. Doolan CJ (2009) Flat-plate interaction with the near wake of a square cylinder. AIAA J 47(2):475–479

16. Ali MSM, Doolan CJ, Wheatley V (2011) Low Reynolds number flow over a square cylinder with a splitter plate. Phys Fluids 23:1–12

17. Ul-Islam S, Rahman H, Abbasi WS, Noreen U, Khan A (2014) Suppression of fluid force on flow past a square cylinder with a detached flat plate at low Reynolds number for various spacing ratios. J Mech Sci Technol 28(12):4969–4978

18. Wang JS, Xu YK, Cheng HJ (2016) Features of flow past square cylinder with a perforated plate. Trans Tianjin Univ 22(6):544–554

19. Qian YH, Humières D, Lallemand P (1992) Lattice BGK models for Navier–Stokes equation. Europhys Lett 17(6):479–484

20. Lumley JL (1970) Stochastic tools in turbulence. Academic, New York

21. Sirovich L (1987) Turbulence and the dynamics of coherent structures part I: coherent structures. Q Appl Math XLV(3):561–571

22. Liang YC, Lee HP, Lim SP, Lin WZ, Lee KH, Wu CG (2002) Proper orthogonal decomposition and its applications-part I: theory. J Sound Vib 252(3):527–544

23. Holmes P, Lumley JL, Berkooz G (1996) Turbulence coherent structures, dynamical systems and symmetry. Cambridge University Press, Cambridge

24. Berkooz G, Holmes P, Lumley JL (1993) The proper orthogonal decomposition in the analysis of turbulent. Annu Rev Fluid Mech 25:539–575

25. Guo ZL, Zheng CG, Shi BC (2002) Non-equilibrium extrapolation method for velocity and boundary conditions in the lattice Boltzmann method. Chin Phys 11(4):0366–0374

26. Mushyam A, Bergada JM (2017) A numerical investigation of wake and mixing layer interactions of flow past a square cylinder. Meccanica 52(1–2):107–123

27. Breuer M, Bernsdorf J, Zeiser T, Durst F (2000) Accurate computations of the laminar flow past a square cylinder based on two different methods: lattice-Boltzmann and finite -volume. Int J Heat Fluid Flow 21:186–196

28. Gera B, Sharma PK, Singh RK (2010) CFD analysis of 3D unsteady flow around a square cylinder. Int J Appl Eng Res 1:3

29. Franke R, Rodi W, Schönung B (1990) Numerical calculation of laminar vortex-shedding flow past cylinders. J Wind Eng Ind Aerodyn 35:237–257